Two-phonon infrared spectra of Si and Ge: Calculating and assigning features

Eric L. Shirley*
Optical Technology Division, National Institute of Standards and Technology, 100 Bureau Drive, MS 8441, Gaithersburg, Maryland 20899-8441, USA

Hadley M. Lawler
Department of Physics, University of Washington, Box 351560, Seattle, Washington 98195-1560, USA
(Received 10 May 2007; published 16 August 2007)

Third-order density-functional perturbation theory yields the terahertz and/or far-infrared absorption spectra for silicon and germanium, including all two-phonon combination and difference features. Temperature-dependent spectra are compared to available experimental results. Critical-point analysis is used to identify the branch and wave-vector indices of many features.

DOI: 10.1103/PhysRevB.76.054116 PACS number(s): 78.20.Ci, 71.15.−m, 71.55.Cn, 71.15.Mb

INTRODUCTION

Terahertz and far-infrared (far-ir) absorption in insulators because of single, ir-active phonons is a well known effect, although it usually only involves phonons near the Brillouin-zone center and does not occur in materials with sufficiently high symmetry. Direct coupling of phonon oscillator *pairs* to light, on the other hand, which results from higher-order Born effective charges, occurs at sums and differences of phonon frequencies and, in principle, involves phonons everywhere in the Brillouin zone. This was discussed, for instance, in the classic work by Lax and Burstein.[1] In materials such as Si and Ge, two- (and other multi-) phonon absorption is the chief cause of absorption for wavelengths longer than, say, 3 μm. Such absorption spectra can have rich, multi-peaked structure because of Van Hove singularities. However, to be on a sound footing, their detailed interpretation usually requires theoretical calculations yielding definitive replicas of spectral features. Thus, as an analytical tool, absorption spectroscopy complements other methods, including inelastic neutron scattering and Raman scattering. To this end, theoretical modeling of absorption spectra is a good indicator to differentiate intrinsic absorption features from extrinsic ones in the two-phonon spectral region.

Despite the wealth of past studies, many of which are cited here and/or reviewed by Birman,[2] modern electronic structure calculation methods have undergone sufficient recent improvements to warrant further analysis of two-phonon absorption spectra. In particular, density-functional perturbation theory (DFPT)[3] permits (in simple materials) routine accurate calculations of dynamical matrices everywhere in the Brillouin zone, and third-order DFPT (using the "$2n+1$ theorem" of Gonze and Vigneron,[4] as implemented by Debernardi and Baroni[5] and Dal Corso and Mauri[6]) permits reasonable calculation of anharmonic couplings and second-order Born charges. In an earlier work, Deinzer and Strauch[7] studied the far-ir absorption spectra of Si and Ge using DFPT.

In this work, we carry out calculations along the same lines as Deinzer and Strauch.[7] We find theoretical replicas of a very large number of absorption features in Si and Ge in our two-phonon absorption spectra and their temperature dependences. Because of the level of detail we obtain, we go beyond earlier work by carrying out critical-point analysis to assign a large number of distinct absorption features in both materials. We assert that the present assignments are more rigorous than earlier ones, if only because of the available modern electronic structure methods, including the calculation of coupling matrix elements. The results suggest that similar analyses can be carried out for other materials. This should be useful for quantitatively testing the understanding of phonon dispersion in solids and benchmarking the accuracy of electronic structure calculations.

In what follows, we first introduce the formalism used here to describe one- and two-phonon effects in absorption spectra. For simplicity, we restrict much of the discussion to materials with isotropic properties, but this restriction can be lifted in future work with modest elaboration. We describe details of our particular implementation of second- and third-order DFPT, with an emphasis on Brillouin-zone sampling. We then present absorption spectra along with experimental spectra taken from the literature. Finally, we describe and implement a scheme to carry out critical-point analysis, a lot of which was done largely automatically. This led to identifying many critical-point features in Si and Ge, except near the strongest peaks, where several points are so closely spaced that assignment of observed features could be ambiguous and was not attempted. We hope that in some instances, reinvigorated experimental effort will increase the benefit of the present critical-point analysis to characterize phonon spectra at previously unachieved levels of detail.

FORMALISM AND DERIVATION OF DIELECTRIC FUNCTION

To start, say that a crystal has Bravais lattice $\{\mathbf{R}\}$ with unit-cell volume Ω_0. An atom in the cell belonging to lattice vector $\mathbf{R}$ is located at $\mathbf{R}+\boldsymbol{\tau}_A+\mathbf{d}_{A,\mathbf{R}}$, so that $\boldsymbol{\tau}_A$ is the basis vector for sublattice A and $\mathbf{d}_{A,\mathbf{R}}$ is the atom's displacement from equilibrium. One can introduce the discrete Fourier transform $\mathbf{s}_{A,\mathbf{k}}=N^{-1/2}\Sigma_{\mathbf{R}}e^{-i\mathbf{k}\cdot\mathbf{R}}\mathbf{d}_{A,\mathbf{R}}$, where N is the number of unit cells in the crystal, and also the number of values of $\mathbf{k}$. This implies $\mathbf{d}_{A,\mathbf{R}}=N^{-1/2}\Sigma_{\mathbf{k}}e^{+i\mathbf{k}\cdot\mathbf{R}}\mathbf{s}_{A,\mathbf{k}}$. In the harmonic approximation, the dynamical matrix is

$$D^0_{ij}(\mathbf{k}) = (m_i m_j)^{-1/2} \frac{\partial^2 E}{\partial s_{i,-\mathbf{k}} \partial s_{j,\mathbf{k}}}, \tag{1}$$

where E is the total energy. (All derivatives are to be understood as being evaluated at zero displacement and zero electric field.) $\mathbf{D}^0(\mathbf{k})$ has eigenvalues $\{\omega^2_{\mathbf{k}\nu}\}$, where ν specifies a phonon branch and $\omega_{\mathbf{k}\nu}$ is the harmonic frequency, and orthonormal eigenvectors $\{\mathbf{e}_{\mathbf{k}\nu}\}$, and an index i or j specifies a sublattice and Cartesian coordinate.

The potential energy of a crystal has an expansion of the form

$$U = U_0 + \frac{1}{2} \sum_{\mathbf{k}ij} \left[(m_i m_j)^{1/2} s_{i,-\mathbf{k}} s_{j,\mathbf{k}} \left(D^0_{ij}(\mathbf{k}) + \sum_p u_p \frac{\partial D_{ij}(\mathbf{k})}{\partial u_p} \right) \right] + \cdots . \tag{2}$$

$D^0_{ij}(\mathbf{k})$ includes harmonic terms, and accompanying terms go 1 order beyond the harmonic approximation. We consider two such terms. One term describes anharmonic coupling of a zone-center optical mode to phonon pairs. Such a pair can be two phonons with opposite momenta, which are simultaneously emitted or absorbed, or two phonons with equal momenta, of which one is absorbed and one is created. The other term describes coupling of a macroscopic electric field to such pairs. Hence, u_p is either a zone-center normal-mode coordinate or a field strength. We do not consider higher derivatives of the Born-Oppenheimer surface or third derivatives involving three oscillators of which none is at the zone center. In writing the potential energy as above, $D_{ij}(\mathbf{k})$ is a generalization of the dynamical matrix, whereas $D^0_{ij}(\mathbf{k})$ is its (harmonic) value at zero sublattice displacement and electric field.

One can quantize the normal-mode harmonic oscillators, for which we use the following notation. A normalized phonon eigenvector has components describing atomic displacements of the form $q_{\mathbf{R}i,\mathbf{k}\nu} = N^{-1/2} e^{i\mathbf{k}\cdot\mathbf{R}} e_{i,\mathbf{k}\nu}$, with phonon frequency $\omega_{\mathbf{k}\nu}$ and raising and lowering operators $a^+_{\mathbf{k}\nu}$ and $a_{\mathbf{k}\nu}$. The lattice kinetic energy is

$$T = \frac{1}{4} \sum_{\mathbf{k}\nu\nu} \omega_{\mathbf{k}\nu} (a_{-\mathbf{k}\nu} - a^+_{\mathbf{k}\nu})(a^+_{-\mathbf{k}\nu} - a_{\mathbf{k}\nu}), \tag{3}$$

while the harmonic lattice potential energy is

$$U_h = U_0 + \frac{1}{4} \sum_{\mathbf{k}\nu\nu'} (\omega_{\mathbf{k}\nu} \omega_{\mathbf{k}\nu'})^{-1/2} \sum_{ij} (e_{i,\mathbf{k}\nu})^* D^0_{ij}(\mathbf{k}) e_{j,\mathbf{k}\nu'} \times (a_{-\mathbf{k}\nu} + a^+_{\mathbf{k}\nu})(a^+_{-\mathbf{k}\nu'} + a_{\mathbf{k}\nu'}). \tag{4}$$

In the harmonic approximation and at zero electric field, the Hamiltonian is $H_0 = T + U_h = U_0 + \Sigma_{\mathbf{k}\nu} \omega_{\mathbf{k}\nu} (a^+_{\mathbf{k}\nu} a_{\mathbf{k}\nu} + 1/2)$. Coupling of phonon pairs to an electric field or zone-center optical phonon is given by the replacement $D^0_{ij}(\mathbf{k}) \to D^0_{ij}(\mathbf{k}) + \Sigma_p u_p [\partial D_{ij}(\mathbf{k}) / \partial u_p]$ in Eq. (4). This also furnishes the matrix elements.

Henceforth, we assume a two-atom cubic- or tetrahedral-symmetry crystal structure with cubic or tetragonal site symmetry such as diamond, zinc blende, rocksalt, or cesium chloride. In each cell, the atom at site $\boldsymbol{\tau}_1$ has Born effective charge $-Z_{eff}$, and the atom at site $\boldsymbol{\tau}_2$ has Born effective charge $+Z_{eff}$. We can specify the zone-center optical-phonon coordinate in terms of the average relative sublattice displacement, $\mathbf{x} = N^{-1/2}(\mathbf{s}_{2,\mathbf{k}=0} - \mathbf{s}_{1,\mathbf{k}=0})$. It is now standard to use DFPT to calculate $D^0_{ij}(\mathbf{k})$, $\partial D_{ij}(\mathbf{k}) / \partial x_\alpha$, and $\partial D_{ij}(\mathbf{k}) / \partial E_\alpha$. We provide further details of our implementation and references in the next section. One can use the derivatives to construct the coefficients

$$b^\alpha_{\mathbf{k}\nu\nu'} = \sum_{ij} \left(\frac{e_{i,\mathbf{k}\nu}}{(2\omega_{\mathbf{k}\nu})^{1/2}} \right)^* \frac{\partial D_{ij}(\mathbf{k})}{\partial x_\alpha} \left(\frac{e_{j,\mathbf{k}\nu'}}{(2\omega_{\mathbf{k}\nu'})^{1/2}} \right) \tag{5}$$

and

$$m^\alpha_{\mathbf{k}\nu\nu'} = \sum_{ij} \left(\frac{e_{i,\mathbf{k}\nu}}{(2\omega_{\mathbf{k}\nu})^{1/2}} \right)^* \frac{\partial D_{ij}(\mathbf{k})}{\partial E_\alpha} \left(\frac{e_{j,\mathbf{k}\nu'}}{(2\omega_{\mathbf{k}\nu'})^{1/2}} \right). \tag{6}$$

These expressions describe coupling of zone-center phonons and electric fields to phonon pairs, giving the total crystal Hamiltonian,

$$H = H_0 + \frac{1}{2} \sum_{\mathbf{k}\nu\nu',\alpha} (b^\alpha_{\mathbf{k}\nu\nu'} x_\alpha + m^\alpha_{\mathbf{k}\nu\nu'} E_\alpha) \times (a^+_{\mathbf{k}\nu} + a_{-\mathbf{k}\nu})(a^+_{-\mathbf{k}\nu'} + a_{\mathbf{k}\nu'}). \tag{7}$$

For simplicity, if one treats the zone-center optical phonon and radiation field classically, one has

$$\mu \ddot{\mathbf{x}}(t) = \mathbf{F}(t). \tag{8}$$

Here, μ is the reduced mass. The driving force $\pm\mathbf{F}$ on each atom (equal and opposite for members of the two sublattices) arises from the harmonic restoring force, the electric field, and anharmonicity:

$$\begin{aligned} F_\alpha(t) &= -\mu\omega_0^2 x_\alpha(t) + Z_{eff} E_\alpha(t) - (2N)^{-1} \sum_{\mathbf{k}\nu\nu'} b^\alpha_{\mathbf{k}\nu\nu'} (a^+_{\mathbf{k}\nu} + a_{-\mathbf{k}\nu}) \\ &\quad \times (a^+_{-\mathbf{k}\nu'} + a_{\mathbf{k}\nu'}) \\ &= -\mu\omega_0^2 x_\alpha(t) + Z_{eff} E_\alpha(t) - (2N)^{-1} \sum_{\mathbf{k}\nu\nu'} b^\alpha_{\mathbf{k}\nu\nu'} A_{\mathbf{k}\nu\nu'}(t). \end{aligned} \tag{9}$$

The induced polarization is

$$P_\alpha(t) = \Omega_0^{-1} \left[Z_{eff} x_\alpha(t) - (2N)^{-1} \sum_{\mathbf{k}\nu\nu'} m^\alpha_{\mathbf{k}\nu\nu'} A_{\mathbf{k}\nu\nu'}(t) \right]. \tag{10}$$

Above, $A_{\mathbf{k}\nu\nu'}(t)$ is a scaled product of normal-mode coordinates for certain phonon pairs, such as a pair with indices $\mathbf{k}\nu$ and $-\mathbf{k}\nu'$. The potential energy's mixed second derivative with respect to such a pair's normal-mode coordinates is proportional to

$$Q_{\mathbf{k}\nu\nu'}(t) = b^\alpha_{\mathbf{k}\nu\nu'} x_\alpha(t) + m^\alpha_{\mathbf{k}\nu\nu'} E_\alpha(t), \tag{11}$$

as implied by Eq. (7).

The frequency-dependent dielectric tensor may be found according to the following sequence of definitions and substitutions. Let the following notation indicate the time dependence of the electric field and other quantities:

$$E(t) = \int_{-\infty}^{+\infty} \frac{d\omega}{2\pi} E(\omega)\exp(-i\omega t). \tag{12}$$

From linear-response theory, statistical-mechanics considerations, and appropriate notice of Bose statistics for phonons in the harmonic approximation, the ratio of $A_{\mathbf{k}\nu\nu'}(\omega)$ to $Q_{\mathbf{k}\nu\nu'}(\omega)$ is given by

$$\frac{A_{\mathbf{k}\nu\nu'}(\omega)}{Q_{\mathbf{k}\nu\nu'}(\omega)} = \frac{1+n_{\mathbf{k}\nu}+n_{\mathbf{k}\nu'}}{\omega-\omega_{\mathbf{k}\nu}-\omega_{\mathbf{k}\nu'}+i\eta} - \frac{1+n_{\mathbf{k}\nu}+n_{\mathbf{k}\nu'}}{\omega+\omega_{\mathbf{k}\nu}+\omega_{\mathbf{k}\nu'}+i\eta} + \frac{n_{\mathbf{k}\nu}-n_{\mathbf{k}\nu'}}{\omega+\omega_{\mathbf{k}\nu}-\omega_{\mathbf{k}\nu'}+i\eta} - \frac{n_{\mathbf{k}\nu}-n_{\mathbf{k}\nu'}}{\omega-\omega_{\mathbf{k}\nu}+\omega_{\mathbf{k}\nu'}+i\eta}, \tag{13}$$

with average phonon number $n_{\mathbf{k}\nu}=\{\exp[\omega_{\mathbf{k}\nu}/(kT)]-1\}^{-1}$.[8] In what follows, it is convenient to introduce the shorthand $R_{\mathbf{k}\nu\nu'}(\omega)=(2N)^{-1}A_{\mathbf{k}\nu\nu'}(\omega)/Q_{\mathbf{k}\nu\nu'}(\omega)$ as well as

$$z(\omega) = Z_{eff} - \sum_{\mathbf{k}\nu\nu'} (b^{\alpha}_{\mathbf{k}\nu\nu'})^{*} R_{\mathbf{k}\nu\nu'}(\omega) m^{\alpha}_{\mathbf{k}\nu\nu'}. \tag{14}$$

This is a complex, frequency-dependent effective charge, which is treated as a scalar in the present systems. Time-reversal symmetry allows one to use

$$(b^{\alpha}_{\mathbf{k}\nu\nu'})^{*} m^{\beta}_{\mathbf{k}\nu\nu'} = [(b^{\alpha}_{-\mathbf{k}\nu\nu'})^{*} m^{\beta}_{-\mathbf{k}\nu\nu'}]^{*} \tag{15}$$

and

$$R_{\mathbf{k}\nu\nu'}(\omega) = R_{-\mathbf{k}\nu\nu'}(\omega) \tag{16}$$

to retain only the real part of $(b^{\alpha}_{\mathbf{k}\nu\nu'})^{*} m^{\beta}_{\mathbf{k}\nu\nu'}$.

The electric displacement $D_{\alpha}(\omega)$ is related to $E_{\alpha}(\omega)$ in a way that depends on the above lattice-induced polarization and the electronic polarization. We incorporate the electronic polarization into the ir dielectric constant $\varepsilon_{\infty}(\omega)$, which is real and has very little frequency dependence over the spectral range of interest, while $\varepsilon(\omega)$ denotes the total dielectric function. This gives

$$D_{\alpha}(\omega) = \varepsilon(\omega)E_{\alpha}(\omega) = \varepsilon_{\infty}(\omega)E_{\alpha}(\omega) + (4\pi/\Omega_0)\left[z(\omega)x_{\alpha}(\omega) - \sum_{\mathbf{k}\nu\nu'} (m^{\alpha}_{\mathbf{k}\nu\nu'})^{*} R_{\mathbf{k}\nu\nu'}(\omega) m^{\alpha}_{\mathbf{k}\nu\nu'} E_{\alpha}(\omega) \right]. \tag{17}$$

Using

$$x_{\alpha}(\omega) = [\mu(\omega_0^2-\omega^2)+S(\omega)]^{-1} z(\omega)E_{\alpha}(\omega) = X(\omega)z(\omega)E_{\alpha}(\omega), \tag{18}$$

with

$$S(\omega) = \sum_{\mathbf{k}\nu\nu'} (b^{\alpha}_{\mathbf{k}\nu\nu'})^{*} R_{\mathbf{k}\nu\nu'}(\omega) b^{\alpha}_{\mathbf{k}\nu\nu'}, \tag{19}$$

we find

TABLE I. Pseudopotential reference configurations, cutoff radii (bohr), with local angular-momentum channel indicated by "(loc)," and lattice constants a for Si and Ge.

Element	Ref. config.	r_s, r_p, r_d	a (nm)
Si	$[\mathrm{Ne}]3s^2 3p^{0.5} 3d^{0.5}$	1.4, 1.4, 1.3(loc)	0.5360
Ge	$[\mathrm{Cu}^{+}]4s^2 4p^{0.5} 4d^{0.5}$	1.4(loc), 1.4, 1.3	0.5524

$$\varepsilon(\omega) = \varepsilon_{\infty}(\omega) + (4\pi/\Omega_0)\left[z(\omega)X(\omega)z(\omega) - \sum_{\mathbf{k}\nu\nu'} (m^{\alpha}_{\mathbf{k}\nu\nu'})^{*} R_{\mathbf{k}\nu\nu'}(\omega) m^{\alpha}_{\mathbf{k}\nu\nu'} \right]. \tag{20}$$

In the diamond structure, one has $Z_{eff}=0$, but anharmonicity introduces a zone-center optical-phonon self-energy insertion into the two-phonon propagator. This has a small effect on optical spectra, which are dominated by second-order Born charges, but strongly affects the Raman line shape.[9] In other compounds, one can have $Z_{eff}\neq 0$, and anharmonic coupling of the ir-active phonon to phonons at $\pm\mathbf{k}$ broadens the absorption peak[10] and similarly affects the Raman line shape,[11,12] whereas higher-order Born charges can also play a significant role.

ABSORPTION SPECTRUM CALCULATION

We calculated dynamical matrices following the methods of Giannozzi *et al.*[13] and Gonze and Lee.[14] Perturbations to wave functions in the presence of an electric field or atomic displacements were calculated using an explicit sum of admixtures of the lowest several (eight) conduction bands and implicit sum of admixtures of all remaining conduction bands. In this way, solution of the Sternheimer equations involved inversion of matrices with smaller effective condition numbers. Calculations were done in the plane-wave pseudopotential approach[15] in density-functional calculations[16] using the local-density approximation[17] with four valence electrons per atom. We used Hamann-Schlüter-Chiang pseudopotentials[18] with Vanderbilt cutoff functions.[19] Parameters for scalar-relativistic[20] pseudopotentials and lattice constants are tabulated in Table I. It was especially important to use the theoretical lattice constant in Ge, because using the experimental lattice constant tends to imply metallic behavior.[21,22] Our Ge lattice constant is slightly smaller than that found by Moll *et al.*[23] when they omitted the nonlinear core correction,[24] as have we. A 16 Ry plane-wave cutoff gave converged results for Si and Ge. Because the local electron density always corresponded to the Wigner-Seitz radius $r_s>1$ in the solid, Ceperley-Alder correlation[25] was used with the parametrization by Perdew and Zunger,[26] whereas the Vosko-Wilk-Nusair parametrization[27] was used when generating the pseudopotentials.

To calculate the desired third derivatives, we used third-order DFPT. This exploited the $2n+1$ theorem for density-functional theory as derived by Gonze and Vigneron[4] as expressed in the modified form introduced by Debernardi and

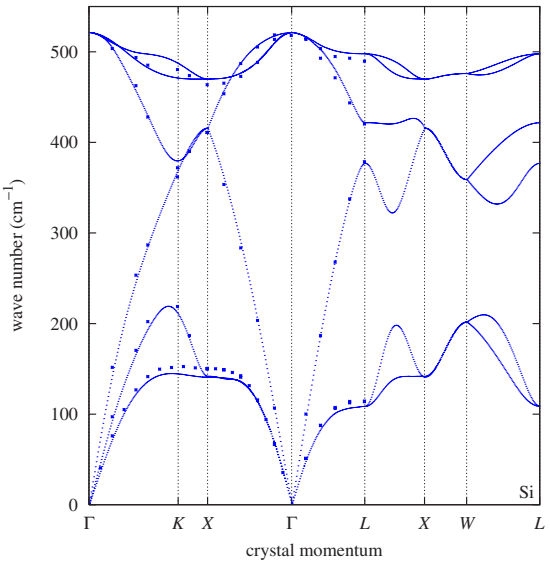

FIG. 1. (Color online) Phonon dispersion in Si vs neutron-scattering data.

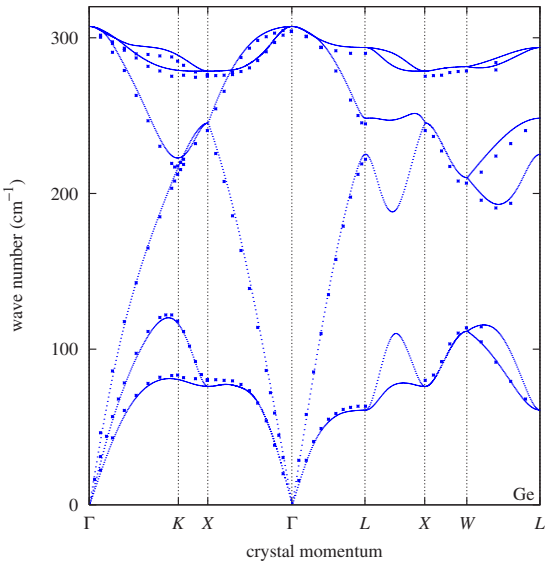

FIG. 2. (Color online) Phonon dispersion in Ge vs neutron-scattering data.

Baroni[5] and Dal Corso and Mauri.[6] Thus, the third derivatives were mixed third derivatives with respect to perturbations in the form of displacement along phonon coordinate at $\mathbf{k}$, displacement along a phonon coordinate at $-\mathbf{k}$, and displacement along an optical-phonon coordinate at the zone center or macroscopic electric field.

By treating sublattice displacements and macroscopic electric fields on an equal footing in the perturbation calculations, the zone-center dynamical matrix, Born effective-charge tensors and the macroscopic polarizability were obtained simultaneously as components of a 9×9 tensor at $\mathbf{k}=0$. We obtained third derivatives related to anharmonicity and second-order Born charges simultaneously when these derivatives involved phonon pairs at nonzero $\pm\mathbf{k}$. Although beyond the scope of this present work, this implies the possibility of calculating the static, nonlinear susceptibility $\chi^{(2)}$ and Raman tensor along the same lines as others.[6,28,29] For the derivatives of $\mathbf{D}(\mathbf{k})$ of interest in this work, we summed the same group of terms as Debernardi,[30] Deinzer *et al.*,[31] and Deinzer and Strauch.[7] Using time-reversal symmetry, though, we explicitly rewrote their expressions to involve only derivatives with respect to perturbations at the zone center and wave vector $\mathbf{k}$, and not wave vector $-\mathbf{k}$ (a device which others may have used implicitly).

We tested our programs according to the following criteria [where below we expand dynamical-matrix indices i,j into sites τ,τ' and coordinates (α,β)]:

(1) calculation of $\mathbf{D}^0(\mathbf{k})$ and phonon dispersion (see Figs. 1 and 2),

(2) satisfaction of the sum rule $\Sigma_{\tau'}D_{\tau\alpha,\tau'\beta}(\mathbf{k}=0)=0$,

(3) satisfaction of the sum rule $\Sigma_{\tau}(\mathbf{Z}^{\tau}_{eff})_{\alpha\beta}=0$,

(4) satisfaction of the sum rule $\Sigma_{\tau}\partial\mathbf{D}(\mathbf{k})/\partial s_{\mathbf{k}=0,\tau\alpha}=0$,

(5) satisfaction of the rule valid in the diamond structure $\partial\mathbf{D}(\mathbf{k}=0)/\partial E_{\alpha}=0$,

(6) anharmonic couplings similar to those obtained by Vanderbilt *et al.*[32] and Debernardi and Baroni,[5]

(7) zone-center optical-phonon self-energy similar to that of Deinzer *et al.*,[31]

(8) null contribution of overtones to absorption spectra in the diamond structure, and

(9) several appropriate symmetries of second- and third-derivative tensors.

In agreement with Giannozzi *et al.*,[13] we foresee the correct Born effective charges (zero in this case) only in the limit of infinite Brillouin-zone sampling. This rule held for first- and second-order Born-effective charges.

In Figs. 1 and 2, we compare phonon dispersions to neutron-scattering data: in Si by Nilsson and Nelin[33] and Dolling,[34] and in Ge by Nilsson and Nelin.[35] Because the calculated dispersion curves rely on the harmonic approximation, interpreting the present comparison warrants the customary caveats.

In Ge, we found that the derivative $\partial\mathbf{D}(\mathbf{k})/\partial E_{\alpha}$ converged very slowly with respect to zone sampling. This appeared to result from a contribution in Brillouin-zone sums over electron states that arose in DFPT that was strongly peaked when it involved states near the zone center. This is plausible because of the small, dipole-allowed local-density approximation band gap at Γ in Ge. Likewise, $\partial\mathbf{D}(\mathbf{k})/\partial E_{\alpha}$ for $\mathbf{k}$ near L (especially along Λ) in Ge and near the X point in Si converged relatively slowly with respect to Brillouin-zone sampling.

To improve the effective convergence with respect to zone sampling, we applied the following strategy. First, we calculated $\mathbf{D}^0(\mathbf{k})$, $\partial\mathbf{D}(\mathbf{k})/\partial x_{\alpha}$, and $\partial\mathbf{D}(\mathbf{k})/\partial E_{\alpha}$ on regular $n\times n\times n$ grids in the Brillouin zone, which correspond to $N=n^3$ total sampling points, including the zone center. (Symmetry was used to unfold results obtained within the irreducible Brillouin-zone wedge.) In Si, we used $n=6$, $n=8$, and $n=10$. In Ge, we used $n=6$, $n=8$, $n=10$, and $n=12$. Such calculations involved sampling electron states on the same grids, so that $\mathbf{k}$ (modulo umklapps) was always a difference vector between points on the grids.

Next, we carried out the discrete Fourier transform to obtain the real-space derivatives, $M(\mathbf{R},N)$

$=N^{-1}\Sigma_{\mathbf{k}} \exp(i\mathbf{k}\cdot\mathbf{R})M(\mathbf{k},N)$, where $M(\mathbf{k},N)$ is the N-dependent $\mathbf{D}^0(\mathbf{k})$, $\partial\mathbf{D}(\mathbf{k})/\partial x_\alpha$, or $\partial\mathbf{D}(\mathbf{k})/\partial E_\alpha$. $\mathbf{D}^0(\mathbf{k})$ and its corresponding phonon dispersion appeared well converged with respect to N at the largest value of N in each compound. Thus, we constructed it from $\{\mathbf{D}^0(\mathbf{R},N)\}$ corresponding to the largest value of N. However, we extrapolated its derivatives to $N=\infty$ using $\{M(\mathbf{R},N)\}$ at two values of N and the hypothesis

$$\mathbf{M}(\mathbf{R},\infty) \approx \mathbf{M}(\mathbf{R},N) + \mathbf{M}_1(\mathbf{R})/N, \tag{21}$$

or using $\{M(\mathbf{R},N)\}$ for three values of N and the hypothesis

$$\mathbf{M}(\mathbf{R},\infty) \approx \mathbf{M}(\mathbf{R},N) + \mathbf{M}_1(\mathbf{R})/N + \mathbf{M}_2(\mathbf{R})/N^2, \tag{22}$$

where $\mathbf{M}(\mathbf{R},\infty)$ and $\{\mathbf{M}_i(\mathbf{R})\}$ uniquely satisfy Eq. (21) or Eq. (22) simultaneously for all values of N used. To do this, we retained $\{M(\mathbf{R},N)\}$ only for values of $\mathbf{R}$ within the boundary of the smallest $n\times n\times n$ supercell. From $\{M(\mathbf{R},\infty)\} \equiv \{M(\mathbf{R})\}$, we constructed an *interpolated* dynamical matrix or its derivatives at any wave vector along the lines of Giannozzi *et al.*[13] (The extrapolation based on three values may be considered especially robust, because it can correct any combination of linear and quadratic convergence with respect to $1/N$.)

The above extrapolations do not reflect the asymptotic behavior expected in the large-N limit. Instead, we selected them to counter the convergence difficulties mentioned previously and observed apparent behavior over the germane range of N. We obtained consistent results from several extrapolations involving two or three values of N. This suggests that our extrapolations capture the main corrections for using the present range of values of N and provided a robust method of convergence acceleration. Based on cursory analysis of the integrands involved in Brillouin-zone integration, we conjecture that the slow convergence results from a sharply peaked contribution to an integration over the Brillouin zone arising at a high-symmetry point that is always included on the grid and weighted in a manner proportional to $1/N$.

Our final results for the derivatives were extrapolated based on the three largest values of N in each semiconductor. We estimate convergence of results for the absorption spectrum to be better than 5% of the absorption coefficient, and convergence of the phonon self-energy damping to be even better. Finally, we calculated self-energies and absorption spectra using $200\times200\times200$ Brillouin-zone sampling of the interpolated dynamical matrix and its derivatives, which proved to be well converged.

RESULTS AND COMPARISON TO EXPERIMENT

Figures 3 and 4 show the calculated absorption spectra for Si and Ge compared to measurements by Ikezawa and Ishigame[36] and Johnson[37] in Si and Ikezawa and Nanba[38] and Fray *et al.*[39] in Ge. The designation "low temperature," which applies to the lower curve(s) in the top and bottom of each figure, includes a theoretical spectrum with $T=6$ K and experimental spectra with $T\leqslant 20$ K, the latter of which should be similar over that range. Likewise, "room temperature," which applies to the upper curve(s) in the top and bottom of each figure, includes a theoretical spectrum with $T=293$ K and experimental spectra with $292\text{K}\leqslant T\leqslant 295$ K, the latter of which should be similar over that range. The spectra are plotted vertically offset, not to disguise the differences between theory and experiment, but to ease comparison of their corresponding features. Calculated spectra presumably lack some broadening, because of other anharmonicity that we ignore, especially around the strongest features near 610 cm^{-1} in Si and 350 cm^{-1} in Ge.

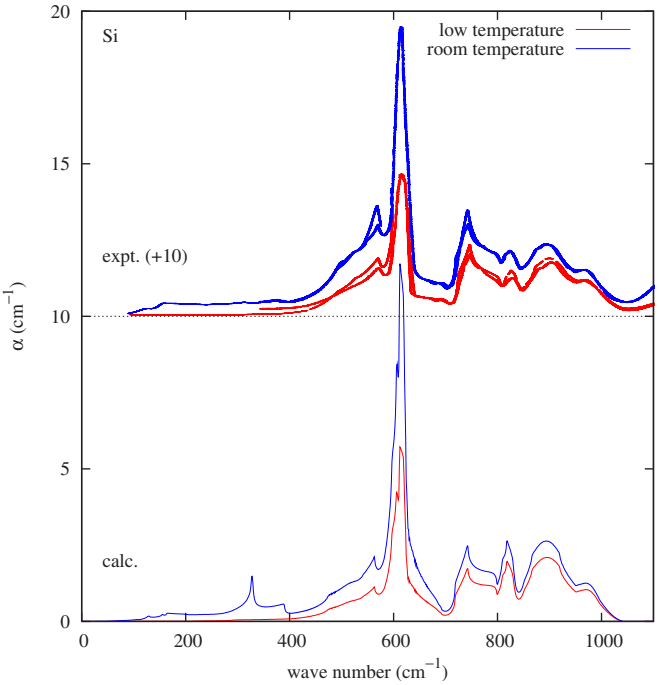

FIG. 3. (Color online) Absorption spectra for Si, taken from experimental references and calculated, at temperature discussed in the text. The top half of the figure (with an offset base line) shows experimental spectra, with the blue, higher family of curves corresponding to room temperature and the red, lower family of curves corresponding to low temperature. The bottom half of the figure is the same, but for theoretical spectra.

The calculations predict shapes and approximate positions of many features well, and their heights are reasonable. The theoretical spectra lack three-phonon features, particularly around and above $2\omega_{TO}$, where ω_{TO} is the zone-center optical-phonon frequency (517 cm^{-1} in Si and 302 cm^{-1} in Ge as measured). Also, critical-point features in Si arising from difference bands, predicted to be at 330 and 389 cm^{-1} (but observed at 315 and 374 cm^{-1}), are far too strong. Critical-point analysis (described in the next section) suggests that these features arise from critical points near X and U/K for the lower peak and L for the higher peak. Perhaps the calculation's exaggerated flattening of the transverse acoustic phonon dispersion near those points contributes to their overestimated strength.

CRITICAL-POINT ASSIGNMENT OF SPECTRAL FEATURES

We applied critical-point analysis to identify branches and wave vectors of phonon combinations and differences giving

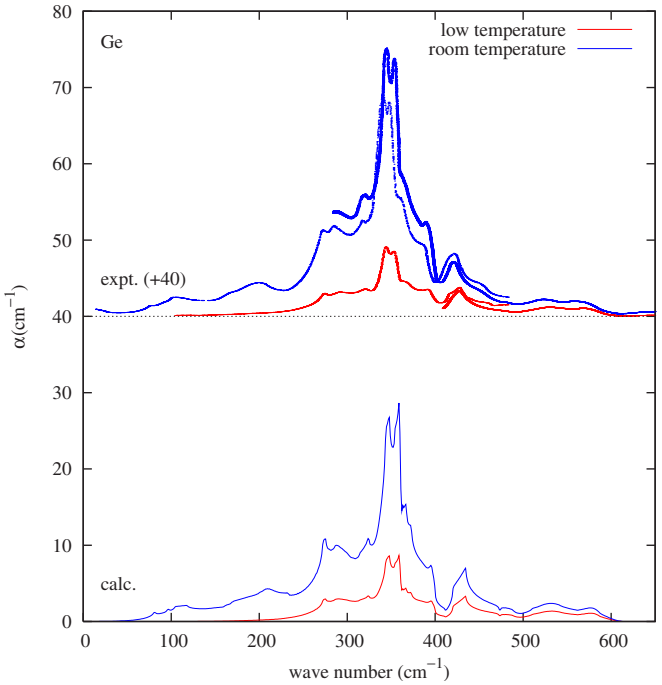

FIG. 4. (Color online) Absorption spectra for Ge, taken from experimental references and calculated, at temperature discussed in the text. The top half of the figure (with an offset base line) shows experimental spectra, with the blue, higher family of curves corresponding to room temperature and the red, lower family of curves corresponding to low temperature. The bottom half of the figure is the same, but for theoretical spectra.

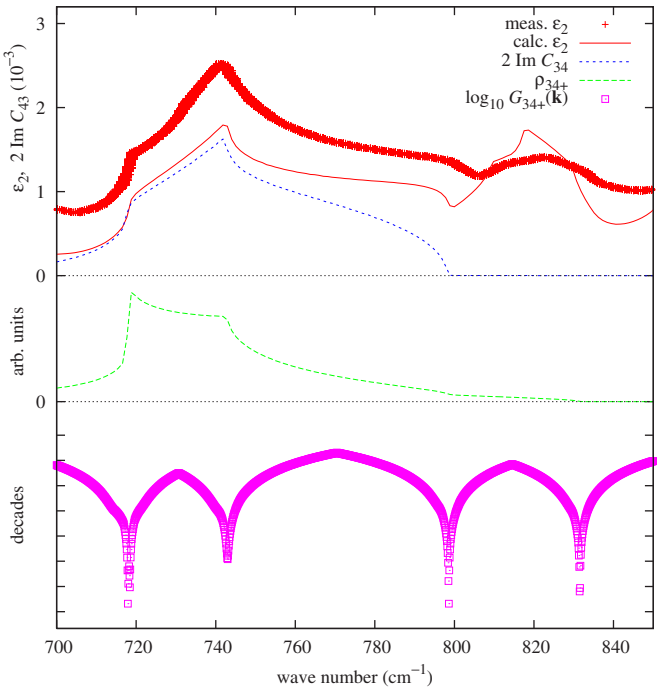

FIG. 5. (Color online) Top panel: Imaginary part of dielectric function ε_2 as measured (red crosses), calculated (red curve), and contribution from combinations of branches 3 and 4 (blue dashed curve). Middle panel: Two-phonon density of states for combination of branches 3 and 4. Bottom panel: Semilogarithmic scatter plot of the magnitude of gradient of branch combination frequency vs frequency for various crystal momenta.

rise to several spectral features. While the calculations do not improve on the accuracy of measurements, critical-point analysis can complement measurements and help one obtain more information from them. Critical-point analysis is discussed in several references cited below, and described in great detail in Birman's papers[40,41] and book.[2] In the following critical-point analysis, we seek to assign discontinuities of slope of the spectra, resulting from local extrema or saddle points of $\omega_{\mathbf{k}\nu} \pm \omega_{\mathbf{k}\nu'}$. Critical points help one determine frequency sums and differences at discrete places in the Brillouin zone, although the absorption spectra are continua. Because a sum or difference is stationary with respect to small changes in $\mathbf{k}$ at a critical point, a critical-point energy is close to a frequency sum or difference in a *region* of the Brillouin zone, and identifying the point's precise location can be subtle. In particular, truncation of $\{\mathbf{D}^0(\mathbf{R})\}$ with respect to $\mathbf{R}$ could induce Gibbs' oscillations that perturb the crystal momenta of theoretical critical points without strongly affecting their spectral signature.

At a given $\mathbf{k}$, frequency sums and differences for two branches ν and ν' contribute to the absorption spectrum with matrix elements equal except for thermal factors. However, critical points for the sum and difference can occur at different $\mathbf{k}$. High-frequency sums typically exhibit small temperature dependence at low T, and *only* sums occur at very low T because of phonon oscillator Bose statistics. While special-purpose calculations of different portions of the absorption spectrum can isolate sum and difference contributions, the temperature dependence of measured spectra helps differentiate them as well. For all of these reasons, we have carried out separate critical-point analyses for combinations and differences.

To help identify critical points, we introduce the quantities

$$C_{\nu\nu'+}(\omega) + C_{\nu\nu'-}(\omega) = -(4\pi/\Omega_0)\sum_{\mathbf{k}} (m^{\alpha}_{\mathbf{k}\nu\nu'})^* R_{\mathbf{k}\nu\nu'}(\omega) m^{\alpha}_{\mathbf{k}\nu\nu'}, \tag{23}$$

such that $C_{\nu\nu'+}(\omega)$ includes terms with frequency sums and $C_{\nu\nu'-}(\omega)$ includes terms with frequency differences. We note

$$\mathrm{Im}\,\varepsilon(\omega) \approx \sum_{\nu\nu' s} \mathrm{Im}\, C_{\nu\nu' s}(\omega). \tag{24}$$

Here, s indicates a sign. Deinzer and Strauch[7] also consider such decomposition, whereas others have often used the (thermally weighted) two-phonon sum- and difference-frequency densities of states contributing to $\mathrm{Im}\,\Sigma_{\mathbf{k}} R_{\mathbf{k}\nu\nu'}(\omega)$ in critical-point analysis without matrix elements. Plotting $\mathrm{Im}\, C_{\nu\nu' s}(\omega)$ on the same scale as $\mathrm{Im}\,\varepsilon(\omega)$ helps establish more rigorously how strongly various combinations and differences couple to light and the energies at which branches cross in various regions of the Brillouin zone. For instance, the "fifth" branch can be a "transverse optical" or "longitudinal optical" phonon, depending on $\mathbf{k}$. Rather than insisting on maintaining the latter imprecise labels, we merely note the numerical values of a probable $\mathbf{k}$, ν, and ν' for the various critical points, so that degeneracies and symmetries can

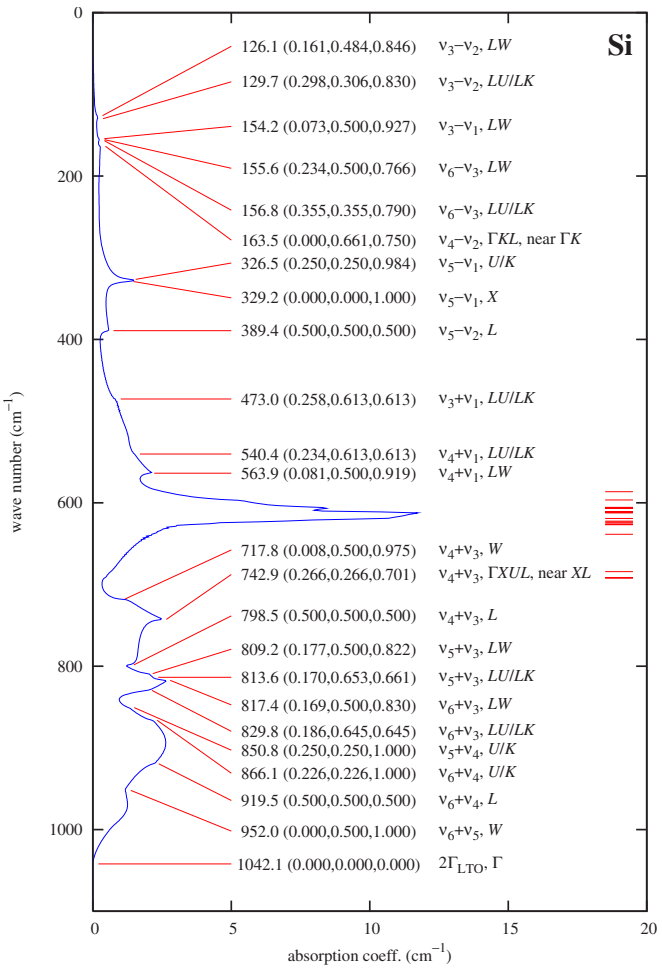

FIG. 6. (Color online) Assignments of critical-point features in Si as discussed in text. The hashes on the right side indicate positions of closely spaced unassigned points.

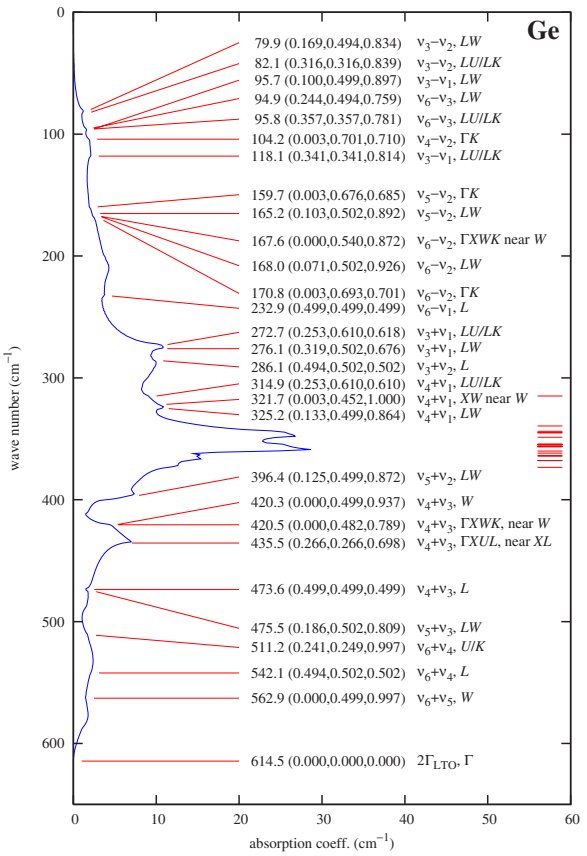

FIG. 7. (Color online) Assignments of critical-point features in Ge as discussed in text. The hashes on the right side indicate positions of closely spaced unassigned points.

imply other equally valid designations. We restrict this endeavor to strong, isolated spectral features, and especially (though not entirely) those with observed counterparts. It would be surprising if future high-resolution measurements could confirm predicted critical points not yet detected experimentally. The relative ease of absorption measurements in these spectral regions for Si and Ge should, however, motivate continual examination of such excellent crystals.

If the above analysis identifies two branches as candidates contributing to a given critical-point feature, a scatter plot of $G_{\nu\nu'\pm}(\mathbf{k})=|\nabla_{\mathbf{k}}(\omega_{\mathbf{k}\nu}\pm\omega_{\mathbf{k}\nu'})|^2$ vs $\omega_{\mathbf{k}\nu}\pm\omega_{\mathbf{k}\nu'}$ for all $\mathbf{k}$ helps reveal the true critical points. We sampled $G_{\nu\nu'\pm}(\mathbf{k})$ on a three-dimensional wave-vector grid with spacings of 0.005 bohr^{-1} along each Cartesian direction, and evaluated it using first-order perturbation theory by differentiating $\mathbf{D}^0(\mathbf{k})$ numerically. This prevented spurious effects from branch degeneracies or crossings. We did not carry out second-derivative analysis of the critical points to completion (to distinguish maxima, minima, and saddle points), but our partial analysis suggests that it would be wise to use second-order perturbation theory to evaluate second derivatives in order to prevent similar spurious effects.

Isolation of results with vanishing $G_{\nu\nu'\pm}(\mathbf{k})$ confirms previous insight into the energy and location of critical points in the irreducible Brillouin-zone wedge.[37] Three-dimensional rendering of their locations suggests that critical points in Si and Ge are disproportionately located, with increasing likelihood, near the (1) faces of, (2) high-symmetry lines (including *LW*) and edges of, and (3) vertices of the wedge. This is fitting, because such entities can lie within the corresponding number of intersecting reflection planes. In diamond and certain other structures, this is tempered by the structure factor and concomitant forbidden reflections.

Figure 5 illustrates critical-point analysis for sum frequencies involving branches 3 and 4 in Si. Between 700 and 850 cm^{-1}, this combination couples to light over a portion of the Brillouin zone, as the comparison of $\varepsilon_2(\omega)$, 2 Im $C_{34+}(\omega)$, and $\rho_{34+}(\omega)$ indicates. Analysis of $G_{34+}(\mathbf{k})$ indicates three theoretical critical points suggested by measured spectra, including a saddle point at or near *W* (718 cm^{-1}), a saddle point between *X* and *L* on the surface of the wedge (743 cm^{-1}), and a local maximum at or near *L* (798 cm^{-1}). (Note that the signed distribution of the relative variation of $\omega_{\mathbf{k}\nu}\pm\omega_{\mathbf{k}\nu'}$ near a critical point can indicate an extremum vs saddle point. Second-derivative analysis would be the preferred method for a definitive indication.) Experimentally, the features are at slightly different energies and have slightly different heights from those calculated, even after allowing for three-phonon effects.

Figures 6 and 7 show transposed theoretical spectra with many critical-point features assigned using the above

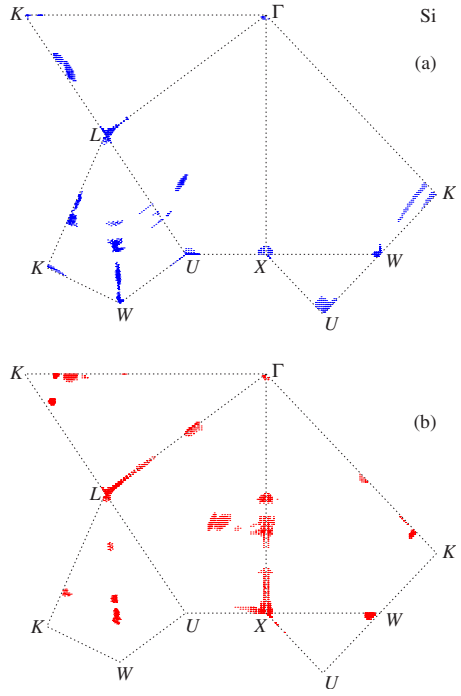

FIG. 8. (Color online) For Si: (a) location of assigned critical points projected onto the surface of the irreducible Brillouin-zone wedge and (b) location of unassigned critical points projected onto the surface of the irreducible Brillouin-zone wedge.

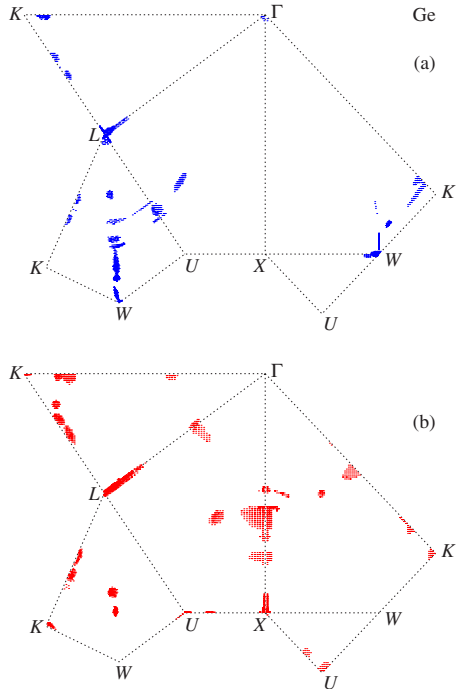

FIG. 9. (Color online) For Ge: (a) location of assigned critical points projected onto the surface of the irreducible Brillouin-zone wedge and (b) location of unassigned critical points projected onto the surface of the irreducible Brillouin-zone wedge.

scheme. The points chosen for assignment are those that appear most identifiable in observed spectra. In particular, we leave most critical-point features over two ranges unassigned: 565–710 cm^{-1} in Si and 310–390 cm^{-1} in Ge. In these ranges, critical points are closely spaced and/or lack individual, identifiable experimental counterparts, but their energies are indicated by dashes on the right side of each figure. Several other critical points that may appear visible also remain unassigned, either because of a lack of a clear experimental counterpart or difficulty in making a likely assignment. For the above two ranges, we merely note that they tend to emphasize combinations of optic and acoustic phonons near the zone boundary (where the acoustic branches tend to flatten).

For the assigned critical points, the labeling includes the *theoretical* critical-point wave number, $1/\lambda(\mathrm{cm})$, approximate Cartesian location in units of $2\pi/a$, where a is the lattice constant, a possible branch combination or difference, and a qualitative description of a familiar geometrical entity (e.g., X) near the critical point. An entity can be a point, line segment (indicated by its end points), or a polygonal facet of the irreducible wedge (indicated by its vertices). We separate equivalent features with a solidus. In Si and Ge, most of the critical points appear to lie on or within 0.03 $bohr^{-1}$ of the wedge surface.

Figures 8 and 9 show the locations of a larger set of (theoretically) ir-active critical points on or projected onto the nearest surface of the wedge. In the top part of each figure, the location of each labeled critical point is indicated by showing a scatter of points with $G_{\nu\nu'\pm}(\mathbf{k})$ below some value that compromises localization and visualization of constant-$G_{\nu\nu'\pm}(\mathbf{k})$ surfaces in the figure. (The locations are already indicated in Figs. 6 and 7.) In the bottom of each figure, approximate locations of all other critical points calculated to have ir activity are indicated. The figures could be cut and folded into the shape of the wedge surface to illustrate the locations in three dimensions. In Si and Ge, many

TABLE II. Critical-point assignments in past work (this work) for Si.

Reference	$1/\lambda$ (cm^{-1})	Assignment
II	375±10 (389.4)	$\mathrm{TO}-\mathrm{TA}, L(\nu_5-\nu_2, L)$
	313±9 (329.2)	$\mathrm{TO}-\mathrm{TA}, X(\nu_5-\nu_1, X)$
KBW	467 (473.0)	$\nu_3+\nu_1, LKW(\upsilon_3+\upsilon_1, LU/LK)$
	520 (see text)	$\nu_1+\nu_4, LKW$ (see text)
	711 (717.8)	$\nu_3+\nu_4, \approx 0.94K(\nu_4+\nu_3, W)$
	738 (742.9)	$\upsilon_3+\nu_4, K(\nu_4+\nu_3, \Gamma XUL, \text{near } XL)$
	818 (817.4)	$\nu_3+\nu_5, K(\upsilon_6+\upsilon_3, LW)$
	908 (919.5)	$\nu_4+\nu_6, L(\upsilon_6+\nu_4, L)$
J	740 (742.9)	$\mathrm{LO}+\mathrm{LA}, -(\nu_4+\nu_3, \Gamma XUL, \text{near } XL)$
JL	917 (919.5)	$\mathrm{TO}+\mathrm{LO}, L(\upsilon_6+\nu_4, L)$
	800 (798.5)	$\mathrm{LO}+\mathrm{LA}, L(\nu_4+\nu_3, L)$
BN	965 (952.0)	$\mathrm{TO}+\mathrm{TO}, W(\upsilon_6+\nu_5, W)$
	902 (919.5)	$\mathrm{TO}+\mathrm{LO}, L(\upsilon_6+\nu_4, L)$
	780 (798.5)	$\mathrm{LO}+\mathrm{LA}, L(\nu_4+\nu_3, L)$

TABLE III. Critical-point assignments in past work (this work) for Ge.

Reference	$1/\lambda$ (cm^{-1})	Assignment
KBW	265 (272.7,276.1)	$\nu_1+\nu_3, LKW(\nu_3+\nu_1, LU/LK, LW)$
	311 (321.7)	$\upsilon_2+\upsilon_3, W(\nu_4+\nu_1, XW$ near $W)$
	396 (396.4)	$\nu_2+\nu_5$, near $LW(\nu_5+\nu_2$, near $LW)$
	417 (420.3,420.5)	$\nu_4+\nu_3$, near $W(\nu_4+\nu_3$, at/near $W)$
	475 (475.5)	$\nu_5+\nu_3, LKW(\nu_5+\nu_3, LW)$
	505[a] (511.2)	$\nu_4+\nu_5, \Gamma XWK(\nu_6+\nu_4, U/K)$
FJQW	563 (562.9)	TO+TO, $-(\nu_6+\nu_5, W)$
	423 (420.3,420.5)	LO+LA, $-(\nu_4+\nu_3$, at/near $W)$
	315 (325.2)	LO+TA, $-(\nu_4+\nu_1, LW)$
JL	460 (473.6)	LO+LA, $L(\upsilon_4+\upsilon_3, L)$
	280[b] (286.1)	LA+TA, $L(\nu_3+\nu_2, L)$

[a]Stated to involve a "very flat region" ranging from (0.625,0.625,0) to (1,0.25,0).
[b]From neutron scattering.

critical points are on the line segment LW, which is the mirror axis of the $LUWK$ kite. This justifies featuring LW in phonon and band dispersion plots.

Several papers present critical-point analysis for two-phonon features in Si and Ge: the works by Johnson,[37] Johnson and Loudon,[42] Balkanski and Nusimovici,[43] Fray *et al.*,[39] Kress, *et al.*,[44] and Ikezawa and Ishigame,[36] indicated by acronyms J, JL, BN, FJQW, KBW, and II in Tables II and III that are discussed below. Johnson's paper contains a fairly thorough review of aspects of critical-point analysis in earlier work. Many of these works focus on high-symmetry points or use the technique of plotting sum and difference frequencies on line segments at the intersection of two or more mirror planes in order to locate turning points. As an example, in this work, the 435.5 cm^{-1} feature in Ge and 742.9 cm^{-1} feature in Si are both clearly visible in Figs. 1 and 2 when one considers $\nu_3+\nu_4$ on LX.

In Tables II and III, we note the points of agreement or near agreement with others' work. We indicate the previous work, wave numbers (ours in parentheses), and stated aspects of the assignments (ours in parentheses). In some cases, degeneracy can resolve apparent branch-label discrepancies. Also, slight discrepancy regarding location is suggestive of two-phonon dispersion topologies that are similar to ours on a coarse scale yet different on a fine scale. There are many disagreements and features assigned by others that we have not attempted to assign, for which we refer readers to those references. Conversely, to our knowledge the present work features a relatively extensive assignment of difference features. The fact that several features assigned by others are not assigned here reiterates our fear that further assignments based on our results could be dubious. (We also caution that, because assignments are aided by theoretical input, it is possible that the agreement of our assignment with an earlier work occasionally involves similar defects in two independent calculations.)

A remarkably detailed agreement with Johnson for Si is found on p. 271 of that article, which reads as "The minimum at 80 mm^{-1} on the high energy side of the band at 74 mm^{-1} attributed to longitudinal optic and acoustic phonons may be due to the fact that this combination is forbidden near the zone boundary in the 100 direction." Johnson's conjecture is precisely in keeping with our critical-point analysis and the scenario detailed in Figs. 1, 5, and 6. From our work, it appears that $\nu_3+\nu_4$ exceeds 800 cm^{-1} chiefly in the region described by Johnson, where the pairs' coupling to light vanishes. A corresponding scenario occurs in Ge. Deinzer and Strauch also discuss the features resulting from the combination $\nu_3+\nu_4$ in both materials.

The critical point at 520 cm^{-1} reported by Kress *et al.* in Si also appears in the spectra of Ikezawa and Ishigame and is suggested in other work. While we did not find this to be a critical point, the combinations $\nu_1+\nu_3$ and $\nu_2+\nu_3$ do appear to have a near leveling of the dispersion near W and at a similar energy, suggesting that a potential critical point may possess spurious incipiency in our results. Nonetheless, there is nearly a kink at about the right wave number in Fig. 3, so the signature is still apparent in our spectrum. Also, because of the similarity of this energy to that of the zone-center TO phonon, we also confirmed robustness of this feature in our spectra with respect to including or omitting anharmonic coupling in the calculation.

CONCLUDING REMARKS

In summary, we have used the $2n+1$ theorem within third-order density-functional perturbation theory to compute coupling of two-phonon oscillators to a macroscopic electric field, including some effects because of anharmonic coupling to zone-center phonons. This leads to a reasonable accounting of the terahertz and/or far-ir absorption spectra of Si and Ge. Using critical-point analysis, we have been able to identify branches and crystal momenta for the best resolved, prominent critical-point features in both compounds. The results suggest that similar analysis could be profitable in other materials. At present, we are considering studying polar materials, where zone-center ir-active phonons can also couple to the light and couple to phonon pairs through anharmonicity. In principle, this allows for interference between such an indirect channel for light coupling to phonon pairs and the direct channel central to the present work.

ACKNOWLEDGMENTS

We thank Z. H. Levine, M. Y. Chou, R. M. Martin, S. G. Louie, and X. Gonze for several fruitful discussions and A. Fein, D. Lehane and Z. H. Levine for help in using the Scientific Computing Facility at the National Institute of Standards and Technology.

*Author to whom correspondence should be addressed. FAX: 301-975-2950; eric.shirley@nist.gov

[1] M. Lax and E. Burstein, Phys. Rev. **97**, 39 (1955).
[2] J. L. Birman, *Theory of Crystal Space Groups and Lattice Dynamics* (Springer, New York, 1984).
[3] S. Baroni, S. de Gironcoli, A. Dal Corso, and P. Giannozzi, Rev. Mod. Phys. **73**, 515 (2001).
[4] X. Gonze and J.-P. Vigneron, Phys. Rev. B **39**, 13120 (1989); **44**, 3494 (1991).
[5] A. Debernardi and S. Baroni, Solid State Commun. **91**, 813 (1994).
[6] A. Dal Corso and F. Mauri, Phys. Rev. B **50**, 5756 (1994).
[7] G. Deinzer and D. Strauch, Phys. Rev. B **69**, 045205 (2004).
[8] G. Dolling and R. A. Cowley, Proc. Phys. Soc. London **88**, 463 (1966).
[9] A. Debernardi, S. Baroni, and E. Molinari, Phys. Rev. Lett. **75**, 1819 (1995).
[10] H. M. Lawler and E. L. Shirley, Phys. Rev. B **70**, 245209 (2004).
[11] F. Widulle, T. Ruf, A. Göbel, E. Schönherr, and M. Cardona, Phys. Rev. Lett. **82**, 5281 (1999).
[12] A. Debernardi, Solid State Commun. **113**, 1 (2000).
[13] P. Giannozzi, S. de Gironcoli, P. Pavone, and S. Baroni, Phys. Rev. B **43**, 7231 (1991).
[14] X. Gonze and C. Lee, Phys. Rev. B **55**, 10355 (1997).
[15] W. E. Pickett, Comput. Phys. Rep. **9**, 115 (1989).
[16] P. C. Hohenberg and W. Kohn, Phys. Rev. **136**, B864 (1964).
[17] W. Kohn and L. J. Sham, Phys. Rev. **140**, A1133 (1965).
[18] D. R. Hamann, M. Schlüter, and C. Chiang, Phys. Rev. Lett. **43**, 1494 (1979).
[19] D. Vanderbilt, Phys. Rev. B **32**, 8412 (1985).
[20] D. D. Koelling and B. N. Harmon, J. Phys. C **10**, 3107 (1977).
[21] M. S. Hybertsen and S. G. Louie, Phys. Rev. B **34**, 5390 (1986).
[22] E. L. Shirley, X. Zhu, and S. G. Louie, Phys. Rev. B **56**, 6648 (1997).
[23] N. Moll, M. Bockstedte, M. Fuchs, E. Pehlke, and M. Scheffler, Phys. Rev. B **52**, 2550 (1995).
[24] S. G. Louie, S. Froyen, and M. L. Cohen, Phys. Rev. B **26**, 1738 (1982).
[25] D. M. Ceperley and B. J. Alder, Phys. Rev. Lett. **45**, 566 (1980).
[26] J. P. Perdew and A. Zunger, Phys. Rev. B **23**, 5048 (1981).
[27] S. H. Vosko, L. Wilk, and M. Nusair, Can. J. Phys. **58**, 1200 (1980); S. H. Vosko and L. Wilk, Phys. Rev. B **22**, 3812 (1980).
[28] G. Deinzer and D. Strauch, Phys. Rev. B **66**, 100301(R) (2002).
[29] M. Veithen, X. Gonze, and P. Ghosez, Phys. Rev. B **71**, 125107 (2005).
[30] A. Debernardi, Phys. Rev. B **57**, 12847 (1998).
[31] G. Deinzer, G. Birner, and D. Strauch, Phys. Rev. B **67**, 144304 (2003).
[32] D. Vanderbilt, S. H. Taole, and S. Narasimhan, Phys. Rev. B **40**, 5657 (1989); **42**, 11373 (1990).
[33] G. Nilsson and G. Nelin, Phys. Rev. B **3**, 364 (1971).
[34] G. Dolling, *Proceedings of the Symposium on Inelastic Scattering of Neutrons in Solids and Liquids* (IAEA, Vienna, 1963), p. 37.
[35] G. Nilsson and G. Nelin, Phys. Rev. B **6**, 3777 (1972).
[36] M. Ikezawa and M. Ishigame, J. Phys. Soc. Jpn. **50**, 3734 (1981).
[37] F. A. Johnson, Proc. Phys. Soc. London **73**, 265 (1959).
[38] M. Ikezawa and T. Nanba, J. Phys. Soc. Jpn. **45**, 148 (1978).
[39] S. J. Fray, F. A. Johnson, J. E. Quarrington, and N. Williams, Proc. Phys. Soc. London **85**, 153 (1965).
[40] J. L. Birman, Phys. Rev. **127**, 1093 (1962).
[41] J. L. Birman, Phys. Rev. **131**, 1489 (1963).
[42] F. A. Johnson and R. Loudon, Proc. R. Soc. London, Ser. A **281**, 274 (1964).
[43] M. Balkanski and M. Nusimovici, Phys. Status Solidi **5**, 635 (1964).
[44] W. Kress, H. Borik, and R. K. Wehner, Phys. Status Solidi **29**, 133 (1968).